

Available online at www.sciencedirect.com

SciVerse ScienceDirect

Acta Materialia 61 (2013) 4696–4706

www.elsevier.com/locate/actamat

Atomic-scale compositional characterization of a nanocrystalline AlCrCuFeNiZn high-entropy alloy using atom probe tomography

K.G. Pradeep^a, N. Wanderka^b, P. Choi^a, J. Banhart^b, B.S. Murty^c, D. Raabe^{a,*}

^a Max-Planck-Institut für Eisenforschung GmbH, Max-Planck-Str. 1, 40237 Düsseldorf, Germany

^b Helmholtz-Zentrum Berlin für Materialien und Energie GmbH, Hahn-Meitner-Platz 1, 14109 Berlin, Germany

^c Indian Institute of Technology—Madras, Chennai 600 036, India

Received 16 December 2012; received in revised form 22 March 2013; accepted 28 April 2013

Available online 21 May 2013

Abstract

We have studied a nanocrystalline AlCrCuFeNiZn high-entropy alloy synthesized by ball milling followed by hot compaction at 600 °C for 15 min at 650 MPa. X-ray diffraction reveals that the mechanically alloyed powder consists of a solid-solution body-centered cubic (bcc) matrix containing 12 vol.% face-centered cubic (fcc) phase. After hot compaction, it consists of 60 vol.% bcc and 40 vol.% fcc. Composition analysis by atom probe tomography shows that the material is not a homogeneous fcc–bcc solid solution but instead a composite of bcc structured Ni–Al-, Cr–Fe- and Fe–Cr-based regions and of fcc Cu–Zn-based regions. The Cu–Zn-rich phase has 30 at.% Zn α -brass composition. It segregates predominantly along grain boundaries thereby stabilizing the nanocrystalline microstructure and preventing grain growth. The Cr- and Fe-rich bcc regions were presumably formed by spinodal decomposition of a Cr–Fe phase that was inherited from the hot compacted state. The Ni–Al phase remains stable even after hot compaction and forms the dominant bcc matrix phase. The crystallite sizes are in the range of 20–30 nm as determined by transmission electron microscopy. The hot compacted alloy exhibited very high hardness of 870 ± 10 HV. The results reveal that phase decomposition rather than homogeneous mixing is prevalent in this alloy. Hence, our current observations fail to justify the present high-entropy alloy design concept. Therefore, a strategy guided more by structure and thermodynamics for designing high-entropy alloys is encouraged as a pathway towards exploiting the solid-solution and stability idea inherent in this concept.

© 2013 Acta Materialia Inc. Published by Elsevier Ltd. All rights reserved.

Keywords: High-entropy alloy; Nanocrystalline; Solid solution; Mechanical alloying; Atom probe tomography

1. Introduction

Metallic alloys are often based on one or two major alloying elements with one constituent being the principal (solvent) element and the other constituents in small proportion (solutes) acting as alloying elements for tuning the desired properties [1]. A new class of alloys referred to as “high-entropy alloys” (HEAs) has been suggested; these alloys are defined as having at least five principal elements in equiatomic or near-equiatomic ratios [2]. The initial rationale behind this design concept is to maximize the

configurational entropy of mixing with the aim of stabilizing a solid-solution-based alloy with high hardness, strength and stability at high temperatures [3,4]. Formation of ordered intermetallics and dissociation into multiple phases is usually not desired. Zhang et al. [3] studied the solid-solution phase formation rules for HEAs and stated that for a high-entropy solid solution the absolute value of the enthalpy of mixing should lie between $-2.685\delta - 2.54 < \Delta H_{\text{mix}} < -1.28\delta + 5.44 \text{ kJ mol}^{-1}$. This relation establishes a phenomenological link between the mixing enthalpy and the atomic size parameter (δ). The authors also suggested that δ should be less than 4.6 and the mixing entropy (ΔS_{mix}) should be greater than $1.61R$, where R is the gas constant. Sheng et al. [5] studied the effect of

* Corresponding author.

E-mail address: d.raabe@mpie.de (D. Raabe).

valence electron concentration (VEC) on the stability of body-centered cubic (bcc) or face-centered cubic (fcc) solid solutions in HEAs. Based on the calculations for different HEA compositions, it was reported that for alloys with $VEC \geq 8$, fcc phases are stable, and bcc phases are reported to be stable for $VEC \leq 6.87$ [5].

Several studies have been carried out on hexanary alloy systems such as AlCoCrCuFeNi due to their favorable combination of high hardness, compressive strength and resistance to softening even at 800 °C [6,7]. Many reports have shown that HEAs produced by conventional metallurgical processing routes such as casting tend to form solid-solution phases either with fcc or bcc structures or mixtures of both [2,8]. Singh et al. [9] studied the microstructure of a multicomponent AlCoCrCuFeNi HEA in the as-cast and splat-quenched condition using transmission electron microscopy (TEM) and atom probe tomography (APT). They observed that the splat-quenched alloy had an imperfectly ordered bcc phase, whereas the conventionally cast alloy formed multiple bcc and fcc phases with a dendritic microstructure within the same alloy. Within these phases local compositional fluctuations and segregations within the dendrites for the same and similar compositions were observed at the nanometer scale by APT [9,10]. The splat-quenched equiatomic AlCoCrCuFeNi HEA exhibited better soft magnetic properties than the as-cast material. It was shown that the Cr–Fe–Co-rich regions in the as-cast alloy underwent spinodal decomposition upon ageing which improved the magnetic properties [11].

Nanostructured single-phase solid-solution formation in HEAs synthesized by mechanical alloying has been reported recently [12–14]. The advantage of powder processing is that the alloys containing low/high melting point elements as constituents can be produced economically compared to other processing routes such as casting. Varalakshmi et al. [12] studied the phase formation in nanocrystalline AlCrCuFeTiZn HEA from binary to hexanary compositions using X-ray diffraction (XRD), scanning electron microscopy (SEM) and TEM. The alloy in the as-milled condition exhibited a single bcc phase with crystallite size of about 10 nm. The high-entropy solid solution was stable even after annealing at 800 °C for 1 h and also possessed very high hardness of about 2 GPa. Similar results were obtained for different hexanary alloy systems such as AlCoCuNiTiZn and CoCrFeMnNiW [13]. Also, dissociation into multiple phases during sintering of mechanically alloyed AlCoCrCuFe and CoCrCuFeNi HEA powders have been reported, where the mixing enthalpy was found to play an important role in the segregation of a Cu-rich fcc phase [14]. However, detailed studies on the microstructure evolution and phase formation in nanocrystalline HEAs have not yet been conducted. Moreover, the stability of nanocrystalline phases at high temperatures is not yet well understood.

The present investigation is, therefore, focused on the atomic-scale analysis of phase formation in a multicomponent nanocrystalline AlCrCuFeNiZn HEA synthesized by

mechanical alloying and subsequent hot compaction. Both the as-milled powder and the compacted specimens were investigated using XRD and TEM for phase identification and crystallite size measurements. Composition analysis in the different phases and at the grain boundaries was conducted by APT. Our target is twofold: on the one hand we aim at a better understanding of structures and phases that occur in nanocrystalline HEA; on the other hand we critically evaluate the thermodynamic and kinetic foundations of phase formation and dissociation kinetics in the HEA framework. For this purpose we use our experimental observations to provide suggestions for the further development of the HEA concept. The first aspect to be discussed in that context takes a thermodynamic direction, namely addressing the fact that the stable state of a solid solution is determined by the Gibbs free energy of all competing phases and not by the mixing entropy alone. Second, our current and some previous observations [8,9] show that many HEA systems do not in fact form the claimed homogeneous solid-solution phase but instead tend to dissociate into several phases. We, therefore, aim at confronting the HEA concept with microstructural observations of multiple phase formation in the present case.

2. Experimental

The HEA was synthesized by mechanical alloying of elemental powders of Al, Cr, Cu, Fe, Ni, Zn (purity $\geq 99.5\%$; particle size 45 μm) in equiatomic fractions in a planetary high-energy ball mill (Fritsch Pulverisette P-5) operated at 300 rpm for 20 h with a ball-to-powder weight ratio of 10:1. Tungsten carbide balls of 10 mm in size and tungsten carbide vials were used for mechanical alloying, with toluene acting as the process-controlling agent. Powder samples were taken at regular intervals of 5 h in order to study the alloying behavior during milling. The 20 h milled powder was subjected to hot uniaxial compression using a hydraulic press at 650 MPa and 600 °C for a holding time of 15 min. The compacts produced under this condition had a density of about 94% as measured by Archimedes principle.

The as-milled powder and compacts were characterized using XRD, TEM and APT. XRD patterns were obtained using a Bruker AXS D8 X-ray diffractometer with Cu K_α radiation in Bragg–Brentano θ – 2θ configuration in conjunction with a monochromator. Overlapping XRD peaks were deconvoluted using Lorentz functions. Compacted specimens were mechanically polished with 1 μm diamond suspension prior to XRD analysis.

TEM samples were prepared by mounting a small piece of a sufficiently thin powder compact/sprinkling of powder particles over a conductive graphite paste. Subsequently the paste was applied uniformly over a Mo ring of 3 mm diameter followed by Ar milling [15,16].

The microstructures of the powder and compacted specimens were characterized using a Philips CM 30 transmission electron microscope operated at 300 kV equipped

with an energy-dispersive X-ray (EDX) spectrometer. The beam spot size for EDX microanalysis was typically 10 nm. Crystallite sizes were quantified via XRD peak broadening using the Scherrer equation [17] and also from TEM analysis.

The elemental distribution was investigated by APT which allows three-dimensional mapping of elements with near-atomic resolution and high detection sensitivity [18]. APT samples were prepared using a dual-beam focused ion beam (FIB) (FEI Helios Nanolab 600) following the procedures described in Ref. [19]. To minimize beam damage, a low-energy (5 keV) Ga beam was used for final ion-milling. APT experiments were performed with a local electrode atom probe (LEAP™ 3000X HR, Cameca Instruments), applying a laser energy of 0.4 nJ at a pulse repetition rate of 250 kHz. The tip temperature was kept at about 60 K. The APT data was evaluated using the software IVAS 3.6 provided by Cameca Instruments.

Nanohardness and the reduced indentation elastic modulus of the powder compacted specimens were measured using a Hysitron TriboIndenter TI900. The measurements were carried out at a load of 2500 μN for 10 s. The reported hardness measurements are an average of at least 10 measurements taken on both sides of the same sample.

3. Results

3.1. Mechanically alloyed powder

Based on SEM images, the as-milled powder samples revealed a particle size of approximately $8 \pm 3 \mu\text{m}$. The size measurements were done on powders that were first dispersed in methanol, ultrasonicated, filtered and then dried prior to imaging. These steps were done to avoid agglomerated particles. After this treatment, we observed that the particles had equiaxed shape and a homogeneous size distribution.

XRD patterns of the powder samples of AlCrCuFeNiZn HEA obtained after sequential 5 h milling intervals are shown in Fig. 1a. After 20 h milling, XRD peaks corresponding to a bcc phase were observed with a lattice parameter, $a_{\text{bcc}} = 287 \text{ pm}$. Even though broadening of the peaks represents nanocrystallization of the alloy, the {110} peak is asymmetric with a small shoulder at 43.5° . Upon deconvolution, the presence of a minor phase with maximum intensity at 43.6° was observed as shown in Fig. 1b. Based on the powder diffraction patterns obtained after 5 h milling steps, we observed that an overlapped phase with a peak corresponding to the {111} plane, indicating the presence of a fcc phase with lattice parameter $a_{\text{fcc}} = 367 \text{ pm}$. This phase could not be indexed because of the absence of successive high-index peaks indicating a small fcc phase fraction compared to the bcc phase. The 20 h milled powder had an average crystallite size of

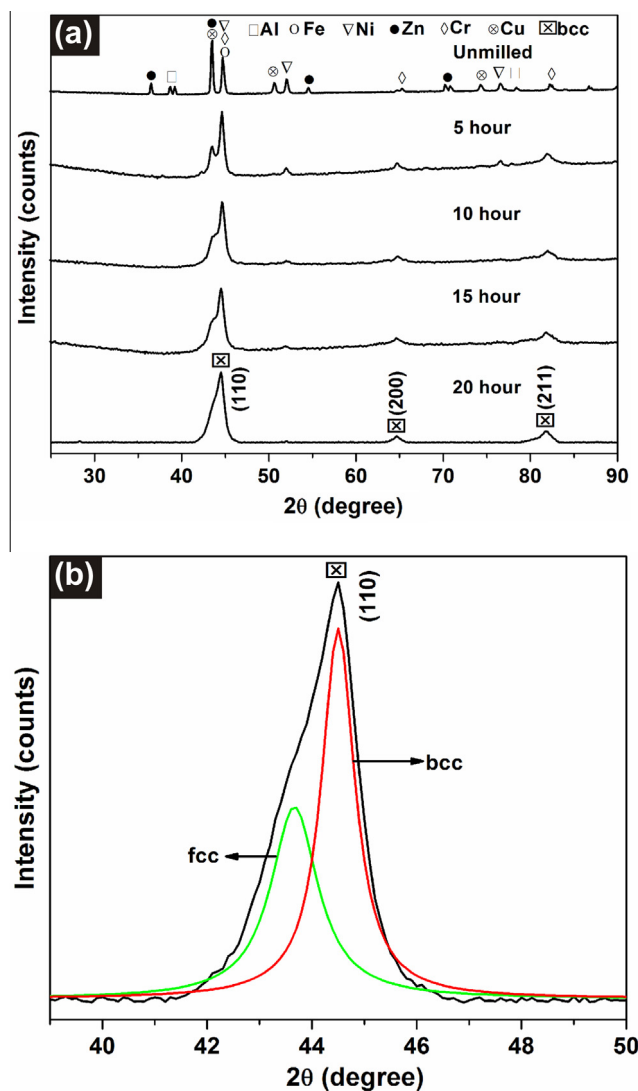


Fig. 1. X-ray diffraction pattern of the AlCrCuFeNiZn HEA powder samples (a) obtained after accumulative milling intervals of 5 h (Cu $K_{\alpha 1}$, $\lambda = 154 \text{ pm}$); (b) deconvoluted high-intensity (110) peak corresponding to the major bcc phase ($a_{\text{bcc}} = 267 \text{ pm}$) obtained after 20 h milling, also showing the presence of a minor fcc phase peak corresponding to the (111) plane with lattice parameter $a_{\text{fcc}} = 367 \text{ pm}$.

$10 \pm 2 \text{ nm}$ with a lattice strain of about 0.75% as measured from the {110} XRD peak after deconvolution.

The dark-field TEM micrograph in Fig. 2a, imaged using the [110] diffraction ring, shows nanocrystals with an average crystallite size of $11 \pm 1 \text{ nm}$. The selected-area electron diffraction (SAED) pattern in Fig. 2b shows diffraction rings corresponding to the bcc phase with $a_{\text{bcc}} = 287 \text{ pm}$ in the 20 h milled condition. Fig. 2c shows a high-resolution (HR) TEM image which confirms the presence of bcc phase with an interplanar spacing of 203 pm corresponding to the bcc [110] plane. Table 1 summarizes the TEM observations and the XRD measurements.

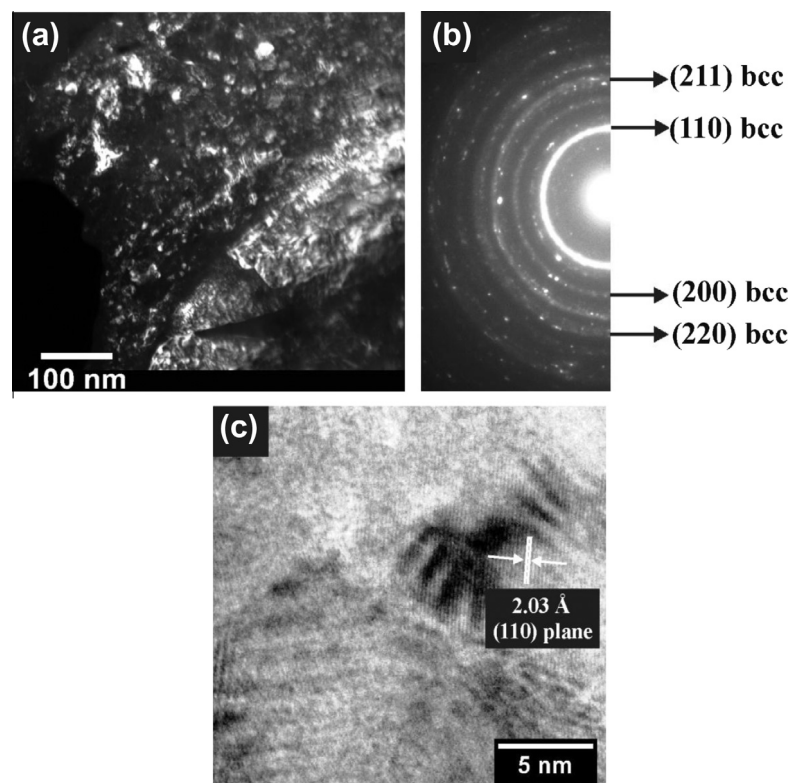


Fig. 2. (a) Dark-field TEM image of the 20 h milled AlCrCuFeNiZn HEA powder using the (110) diffraction ring; (b) corresponding SAED pattern showing the diffraction rings of the bcc phase; (c) HRTEM image of a region with atomic planes corresponding to the bcc phase with an interplanar spacing of 203 pm.

Table 1

Experimental and calculated d -spacing values of the phases present in nanocrystalline equiatomic AlCrCuFeNiZn HEA after 20 h of ball milling and hot compaction (600 °C for 15 min at 650 MPa). The experimental error for the d -spacing values is below 5%.

Angle (2θ) (degree)	d -Spacing (XRD) (pm)	d -Spacing (calculated) (pm)	d -Spacing (TEM) (pm)	(hkl) Planes-crystal structure
<i>Mechanically alloyed powder (20 h milled)</i>				
44.5	203	203	203	(110)-bcc
64.7	144	143	141	(200)-bcc
81.8	117	117	116	(211)-bcc
<i>Hot compacted (600 °C, 650 MPa, 15 min)</i>				
42.69	211	211	213	(111)-fcc
44.47	203	203	203	(110)-bcc
49.69	183	183	183	(200)-fcc
64.63	143	144	146	(200)-bcc
72.87	129	129	135	(220)-fcc
81.88	117	117	114	(211)-bcc
88.28	110	110	108	(311)-fcc

3.2. Hot compacted alloy: structure, composition and nanohardness

Fig. 3 shows the XRD pattern for the 20 h mechanical alloyed powder after (a) annealing at 600 °C for 15 min and (b) after hot compaction at 650 MPa at the same temperature and for the same time. Peaks corresponding to the fcc and bcc phases are obtained in both cases and the phase formation follows the same pattern. Based on peak positions, the lattice parameters of the two phases are determined to be 287 pm for bcc and 367 pm for fcc,

respectively. It should be noted that the intensity of the fcc phase in the annealed condition (Fig. 3a) is lower compared to that of the hot compacted condition (Fig. 3b), indicating their lower volume fraction. Thus the load applied during compaction has accelerated the formation of the fcc phase. However, the parent bcc phase remains the majority phase in both cases. In either case, for the hot compacted condition the bcc phase occupies about 60 vol.% and the fcc phase 40 vol.%. The average crystallite size measured for the phases from these two different treatments is found to be approximately 20 ± 1 nm.

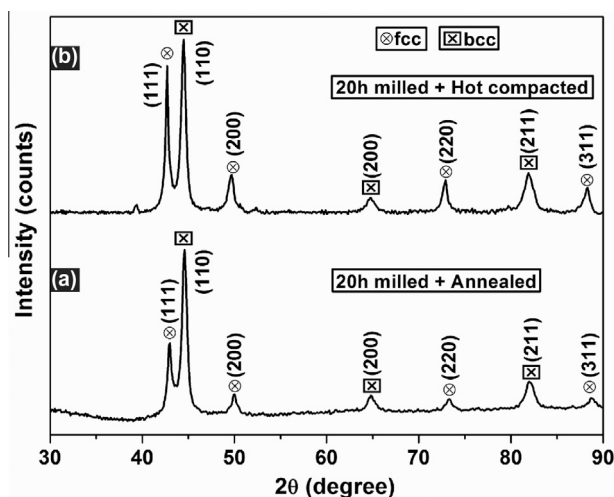


Fig. 3. X-ray diffraction pattern ($\text{Cu } K_{\alpha 1}$, $\lambda = 154 \text{ pm}$) of the 20 h milled AlCrCuFeNiZn HEA powder after: (a) annealing at 600°C for 15 min; (b) hot compaction at 600°C with 650 MPa for 15 min.

A dark-field TEM micrograph imaged using the $[110]$ diffraction ring of the bcc phase is shown in Fig. 4a. Fine nanocrystals of 15–20 nm in diameter are clearly visible. The inset of Fig. 4a displays a histogram of the crystallite size distribution. It can be fitted by a log-normal function with an average crystallite size of $20 \pm 8 \text{ nm}$. The corre-

sponding SAED pattern of the compacted sample is shown in Fig. 4b. The diffraction rings suggest the same bcc and fcc lattice parameters as observed by XRD. Fig. 4c shows the HR TEM image, confirming the presence of the matrix bcc phase with an interplanar spacing of 203 pm corresponding to the distances of the $\{110\}$ planes. Considering the small crystallite size of the nanocrystals, EDX measurements obtained on these samples at various regions for identifying the elemental distribution in each of the phases are not completely reliable and hence are not discussed here. However, in some regions we observed an enrichment of Cu and Zn corresponding to the 30 at.% Zn α -brass composition (see Table 2).

The elemental distribution within the nanocrystals and the chemical composition across different phases and boundaries were obtained from APT. Fig. 5a shows the elemental map of one such measurement, while Fig. 5b displays the individual atomic positions of Al, Cr, Cu, Fe, Ni and Zn in an analyzed volume of $46 \times 46 \times 180 \text{ nm}^3$. All elements are non-uniformly distributed and can be divided into at least two regions based on the enrichment of at least one of the alloying elements. In order to clearly distinguish these regions, a one dimensional concentration–depth profile was plotted (Fig. 6a) using a cylinder of 12 nm radius oriented along the central line through the analyzed volume (inset in Fig. 6a). The error bars represent the 2σ standard deviation. It is obvious from the concentra-

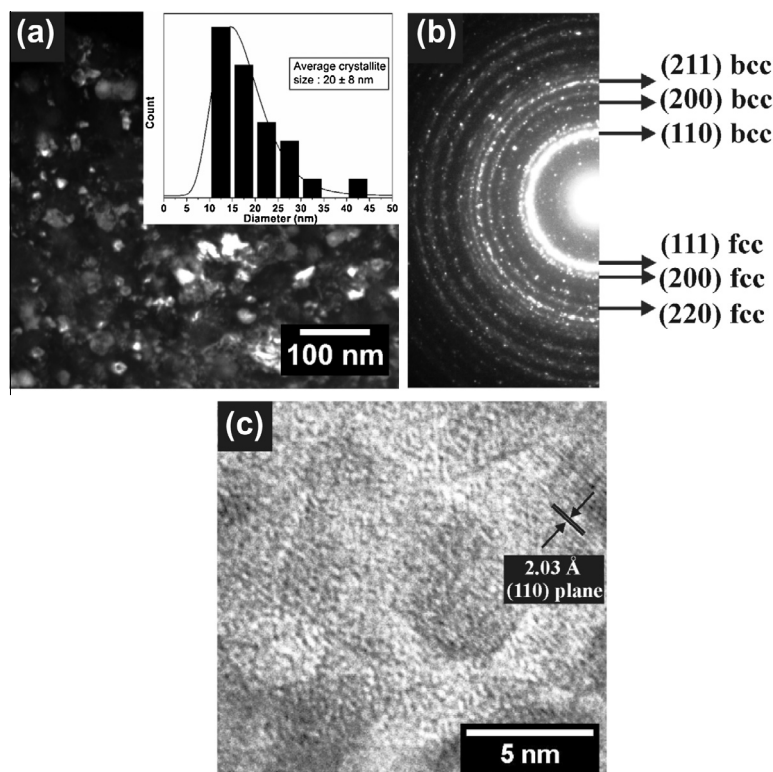


Fig. 4. TEM images of hot compacted (600°C for 15 min at 650 MPa) AlCrCuFeNiZn HEA: (a) dark-field micrograph imaged using the (110) diffraction ring showing fine nanocrystals (inset shows histogram of crystallite size; continuous curve displays fit using log-normal distribution function); (b) corresponding SAED pattern showing the diffraction rings corresponding to the bcc and fcc phases; (c) HRTEM image of a region showing atomic planes corresponding to the bcc phase with an interplanar spacing of 203 pm.

Table 2

Chemical composition of phases (at.%) of mechanically alloyed and hot compacted AlCrCuFeNiZn high-entropy alloy measured by TEM/EDX and by APT. The error bars represent 2σ standard deviation.

Method/region	Enrichment	Al	Cr	Cu	Fe	Ni	Zn
TEM-EDX spot (fcc phase)	Cu	0.7	0.6	63.2	0.7	4.3	30.4
APT 1 (bcc phase)	Ni	18 ± 1.5	–	16 ± 1	6 ± 0.5	43 ± 2	17 ± 1
APT 2 (bcc phase)	Fe	–	0.4 ± 0.1	0.2 ± 0.1	95 ± 0.3	3.2 ± 0.1	0.2 ± 0.1
APT 3 (fcc phase)	Cu	–	–	62 ± 4	–	4.43 ± 2	33.1 ± 3
APT 4 (bcc phase)	Cr	–	86 ± 6	–	14 ± 7	–	–

tion–depth profile that region 1 is enriched in Ni (~ 43 at.%) and region 2 is mainly enriched in Fe (~ 90 at.%). Along the boundaries of Ni-rich and Fe-rich regions, segregation of Cu and Zn (marked by arrows in Fig. 5a and b) having α -brass type composition has been determined which acts as a hetero-interface. It has already been shown from the XRD and TEM measurements that the fcc phase is composed of Cu–Zn. From the concentration–depth profile in Fig. 6a, it is difficult to identify such Cu–Zn enrichment as the segregated area is very thin and the cylinder (12 nm radius) used for the analysis is very large. Hence an isoconcentration surface with 28 at.% Cu is created (rectangle area in inset of Fig. 6b) and from the proximity histogram (Fig. 6b) the local composition of the hetero-interface is determined as listed in Table 2. It should be noted that the concentration of Cr (0.2 at.%) is very low over the entire analyzed volume, which gives rise to speculation that it could be segregated as an almost pure Cr phase similar to that of Fe. In order to verify this hypothesis, several measurements were carried out under the same sample conditions.

Fig. 7 displays the elemental map of another APT measurement of hot compacted AlCrCuFeNiZn HEA, showing the individual atomic positions of Al, Cr, Cu, Fe, Ni and Zn in an analyzed volume of $74 \times 74 \times 46$ nm³. In accordance with the result shown in Fig. 5, all the elements are non-uniformly distributed and can be divided into different regions similar to those in Fig. 5. Considering the morphology of the Cu enrichment, and in order to determine the local chemical composition more accurately, proximity histograms were plotted after creating isoconcentration surfaces as shown in Fig. 8a. In order to maintain consistency in identification, regions enriched in Ni are numbered region 1, while the regions enriched in Cu and Zn are numbered region 3, since the local concentrations of these regions are comparable with the measurement shown in Fig. 5. In addition to Ni-, Fe- and Cu–Zn-rich phases observed in Fig. 5, segregation of Cr atoms along with traces of Fe atoms are identified and are referred to as Cr-rich phase, numbered region 4. The diameters of such regions are about 5–6 nm (see Fig. 8c) with a number density of 4×10^{23} m^{−3}. The term “number density” refers here to the frequency of these zones in the probed APT volume. The local chemical concentrations of such Cr enrichments were determined from the concentration–depth

profile (in Fig. 8d) plotted using a cylinder of 0.65 nm radius oriented along two Cr-rich regions marked in Fig. 8c by a rectangle. Table 2 summarizes the local concentrations in each of these regions together with the TEM/EDX result of the Cu–Zn-rich phase. It could be noted that all the different regions are distinctly partitioned and the sizes of each of these regions are well below 30 nm. The powder compacts had very high hardness in the range of 870 ± 10 HV with an indentation-reduced elastic modulus of 148 ± 20 GPa.

4. Discussion

4.1. High-entropy solid-solution formation

We have successfully synthesized nanocrystalline AlCrCuFeNiZn HEA solid solution by mechanical alloying, and probed the alloying process as a function of milling time. The disappearance of individual elemental XRD peaks and the evolution of solid-solution peaks as shown in Fig. 1a demonstrate gradual alloy formation.

HEAs are by original definition [2–5] suggested to be equiatomic or near-equiatomic multicomponent solid solutions. All elements are solutes and, therefore, the chemical compatibility, i.e. the electronegativity difference and the enthalpy of mixing (ΔH_{mix}) between them, should also be relevant for alloy formation. The high-entropy solid-solution formation rules described above are similar to the Hume–Rothery rules for binary solutions [20]. In the case of AlCrCuFeNiZn HEA the calculated values of the atomic size misfit parameter δ , mixing enthalpy ΔH_{mix} and mixing entropy ΔS_{mix} for this composition are 5.17, -2.5346 kJ mol^{−1} and 14.89 J K^{−1} mol^{−1}, respectively. This confirms the very high mixing entropy of the alloy which is claimed to result in the formation of solid-solution phases. We also observe that this trend is nearly followed, however, only when the material is mechanically alloyed. The values for δ , ΔH_{mix} and ΔS_{mix} were obtained following the formulations and physicochemical parameters described elsewhere [3,21–23]. The calculated phase equilibrium shows that AlCrCuFeNiZn does not fall in a single-phase solid-solution range as anticipated by the HEA rules. Therefore, the as-prepared powder is expected to have a microstructure consisting of a high-entropy solid solution as main phase plus ordered precipitates [23]. This

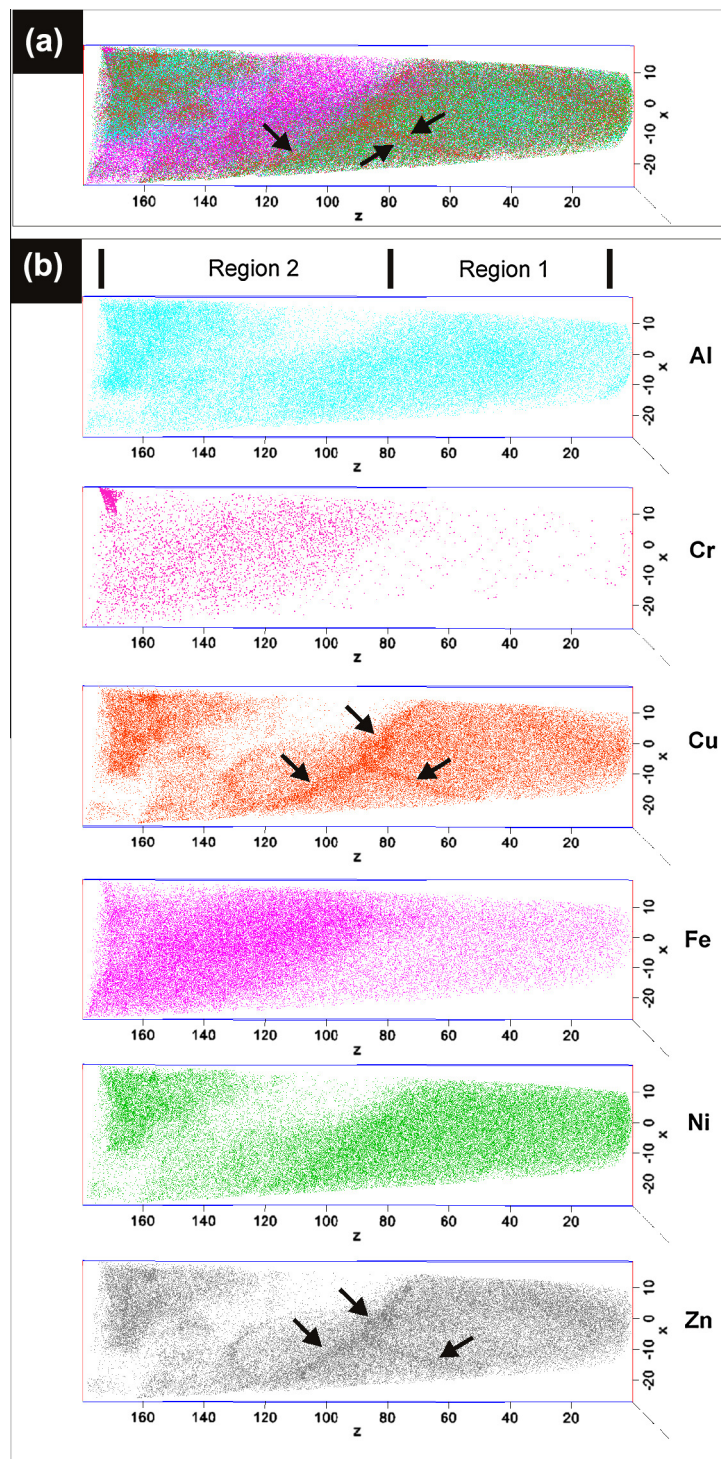


Fig. 5. APT data of hot compacted (600 °C, 650 MPa, 15 min) AlCrCuFeNiZn HEA: (a) elemental map displaying the overall distribution of atoms; (b) three-dimensional reconstruction of individual Al, Cr, Cu, Fe, Ni, Zn atom positions in an analyzed volume of $46 \times 46 \times 180 \text{ nm}^3$. The arrows indicate the segregation of Cu and Zn atoms along the grain boundaries.

matches our findings shown in Fig. 1b, where the as-milled AlCrCuFeNiZn HEA powder contains a major bcc phase along with small fractions of fcc phase. Hence, it can be concluded that the matrix of the AlCrCuFeNiZn HEA is a bcc solid solution (Fig. 2b and c) containing minor precipitated fcc phase fractions. The results obtained from

more equilibrated samples after hot compaction or annealing indeed reveal that a solid solution is not obtained when the system is brought closer to equilibrium. Nevertheless, metallic multiphase alloys can often be rendered into solid solutions when mechanically alloyed (e.g. via ball milling or wire drawing). This non-equilibrium solid-solution state

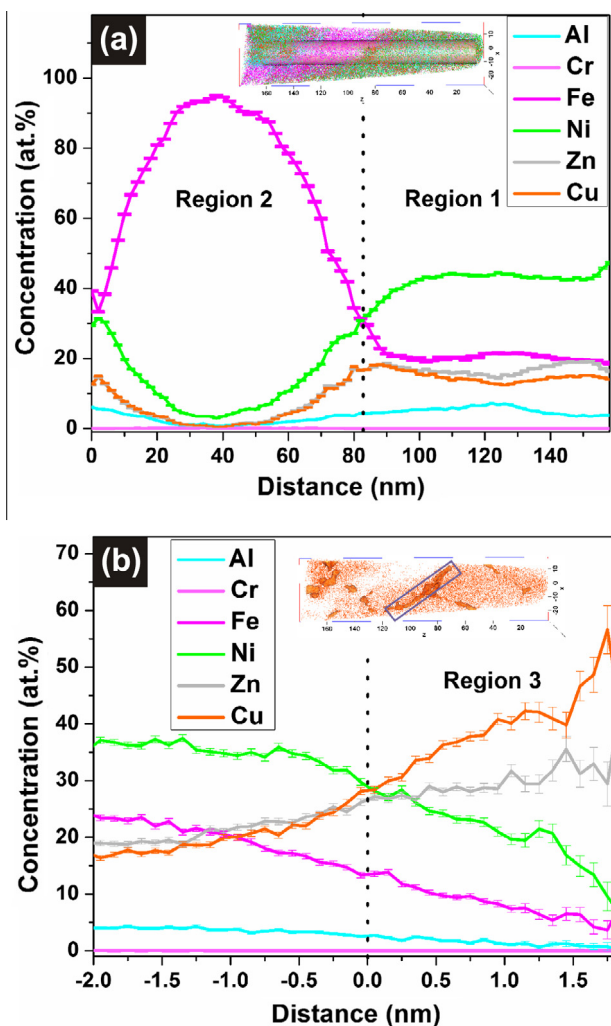


Fig. 6. (a) Concentration–depth profiles of all alloying elements in the hot compacted (600 °C, 650 MPa, 15 min) AlCrCuFeNiZn HEA taken along the analyzed volume of $46 \times 46 \times 180 \text{ nm}^3$ (inset). Concentration values are determined in 2 nm thick slices with a radius of 12 nm. The profiles are plotted with a moving step of 2 nm from right to left. The dotted lines separate regions 1 and 2 which are enriched in Ni and Fe, respectively. (b) Proximity histogram of 0.1 nm bin size with respect to the selected Cu–Zn phase boundary (with 28 at.% Cu interface) marked with a rectangle in the inset.

is promoted by shear-induced mixing during intense co-deformation of initially separated phases [24–29].

4.2. Interphase segregation

Following the gradual progress of mechanical alloying (Fig. 1a), we observe that Cu and Zn segregate into a Cu-rich fcc brass-type phase (Fig. 1b). The formation of this phase can be explained based on the positive enthalpy of mixing of Cu with Fe, Cr and Ni [30]. During hot compaction the fcc phase fraction has increased (40%) with respect to the as-milled condition (12%) as can be seen from the increase in intensity of the fcc peak in Fig. 3b. The lattice parameter of the fcc phase (367 pm) as determined by XRD (Fig. 3b) matches the one measured from

TEM diffraction rings (see Fig. 4b). APT measurements reveal that the composition of the Cu-rich region 3 as indicated in Table 2 (from Figs. 6b and 8b) contains mainly Cu (62–63 at.%), Zn (31–34 at.%) and small amounts of Ni (3–4 at.%). The APT-determined composition of region 3 matches well with the TEM/EDX-measured concentration (see Table 2). Hence, we conclude that region 3 belongs to the minority fcc phase with typical α -brass composition (Cu–30 at.% Zn). The presence of small amounts of Ni is expected to increase the stability of the low melting α -brass phase besides improving its strength [14,31]. A high melting element has as a rule a lower diffusion coefficient in a solid solution than an element with low melting point [32]. Hence, Zn diffusion in the α -brass phase will be relatively high. This explains the formation of α -brass on many interfaces throughout the probed volume, (Fig. 5a and b, see arrows). Since the alloy is nanocrystalline the grain boundary density is very high. This favors segregation of Cu and Zn to the grain boundaries and hence the formation of α -brass (Figs. 5a and 8a).

4.3. Thermally stable hard bcc matrix and discussion of nanocrystalline grain size

The APT analysis reveals that the phases abutting the α -brass-rich interface regions are enriched or respectively depleted in Ni–Al and Cr–Fe (see Figs. 6b and 8d). The formation of a Ni–Al-rich phase is due to the strong interactions of these atoms during mixing, i.e. Ni and Al have the largest negative enthalpy of mixing among all alloying elements, namely -22 kJ mol^{-1} [30]. The values of the energy of formation of the corresponding intermetallic phases are even larger, namely -60 kJ mol^{-1} for the ordered B2 phase NiAl and about -40 kJ mol^{-1} for the L12 phase Ni₃Al. However, the Ni–Al-rich phase also contains substantial amounts of Cu ($\sim 16 \text{ at.}\%$), Zn ($\sim 17 \text{ at.}\%$) and Fe ($\sim 6 \text{ at.}\%$) (see Table 2, region 1). The lattice parameter of the majority bcc phase both in the as-milled and hot compacted condition as measured from the XRD peak positions (Figs. 1a and 3b) and SAED ring pattern (Figs. 2b and 4b) correspond to $a_{\text{bcc}} = 287 \text{ pm}$. A similar Ni–Al phase ($a_{\text{bcc}} = 288 \text{ pm}$) of B2 structure with high amounts of Co, Fe, Cu and Cr has been previously reported for an as-cast AlCoCrCuFeNi HEA [9]. Based on the observation of such enrichments, a near-stoichiometric Ni–Al phase was proposed with different types of sublattice occupations where Fe and Cu were suggested to prefer Al sites, while Cr and Co were assumed to occupy Ni sites [9]. The current HEA has a calculated VEC value of 4.98, and hence the alloy is expected to have a stable bcc phase [5]. This is in accordance with the observation that the bcc Ni–Al phase remains stable even after annealing at 600 °C for 15 min [9]. Therefore, we conclude that the major bcc matrix phase is of Ni–Al type, with other alloying elements occupying specific sublattice positions. Strict long-range intermetallic B2 NiAl ordering, however, cannot be concluded from the current diffraction data, sup-

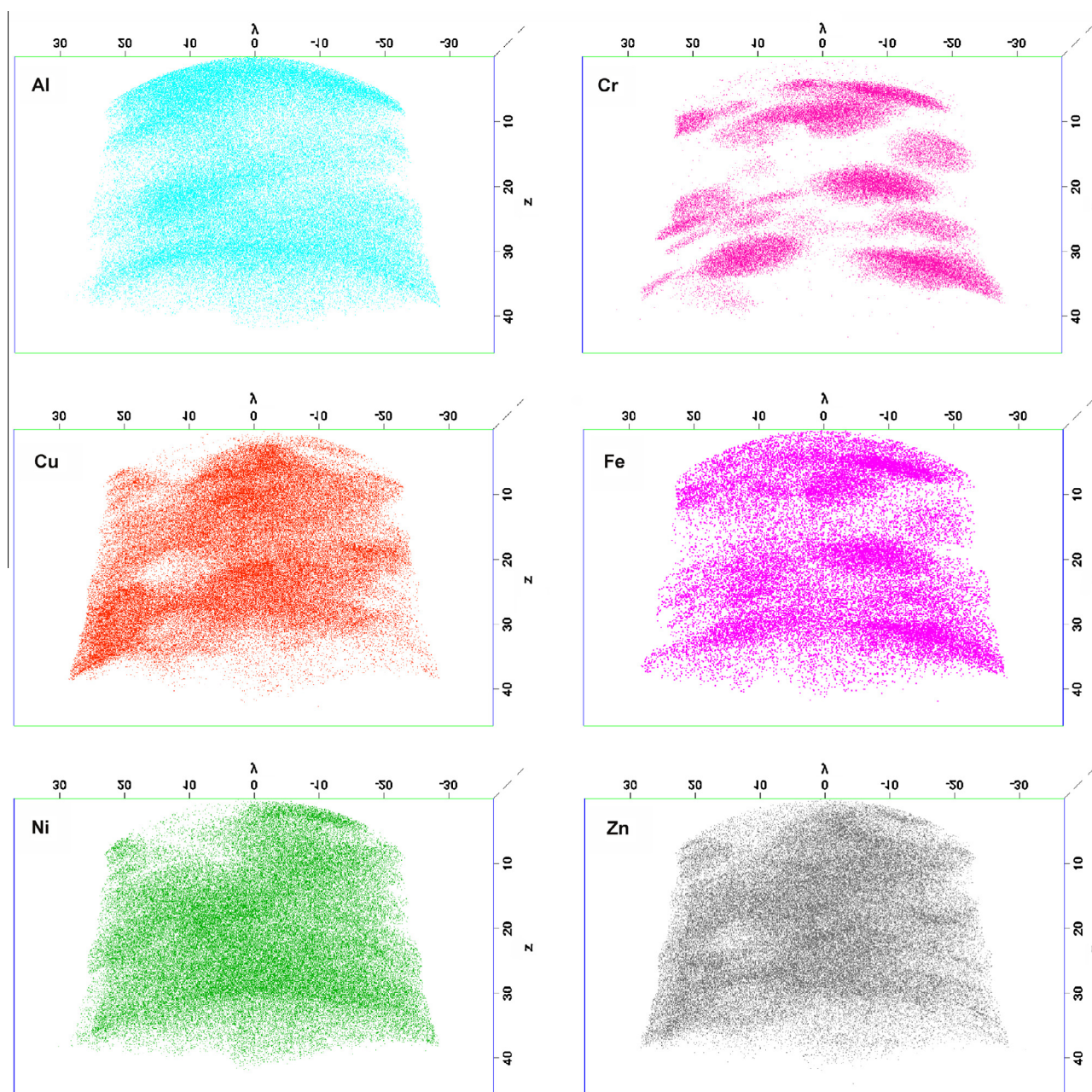


Fig. 7. APT elemental map displaying the atomic positions of Al, Cr, Cu, Fe, Ni and Zn in an analyzed volume of $74 \times 74 \times 46 \text{ nm}^3$ of hot compacted AlCrCuFeNiZn HEA (600 °C, 650 MPa, 15 min).

posingly owing to the variation in the corresponding sub-lattice occupation.

The formation of a Cr–Fe phase in the hot compacted condition (region 4; see Table 2) can also be explained in terms of H_{mix} . With the enthalpy of mixing of Cr–Fe binary system being -1 kJ mol^{-1} it is obvious that these elements tend to segregate into tiny Cr-rich regions of $6 \pm 0.5 \text{ nm}$ in size as shown in Fig. 8c. This effect can also be explained in terms of the low intrinsic diffusion coefficient of the higher melting point element Cr in a solid solution [33]. Chen et al. [33] studied the competition between different elements during mechanical alloying. It was realized that

the elements with higher melting points had a sluggish alloying rate. Accordingly, they observed the segregation of Cr in the form of a separate bcc phase in different HEA systems even after long milling times. In the present case, however, only one type of bcc phase is observed in the as-milled condition (Figs. 1a, 2b and c). This means that mechanical alloying has led to a non-equilibrium bcc solid solution after 20 h milling which upon hot compaction at 600 °C for 15 min has undergone decomposition (probably spinodal) resulting in three chemically different regions but constituting only one bcc phase peak in XRD (Fig. 3b). Spinodal decomposition of the Cr–Fe–Co-rich phase into

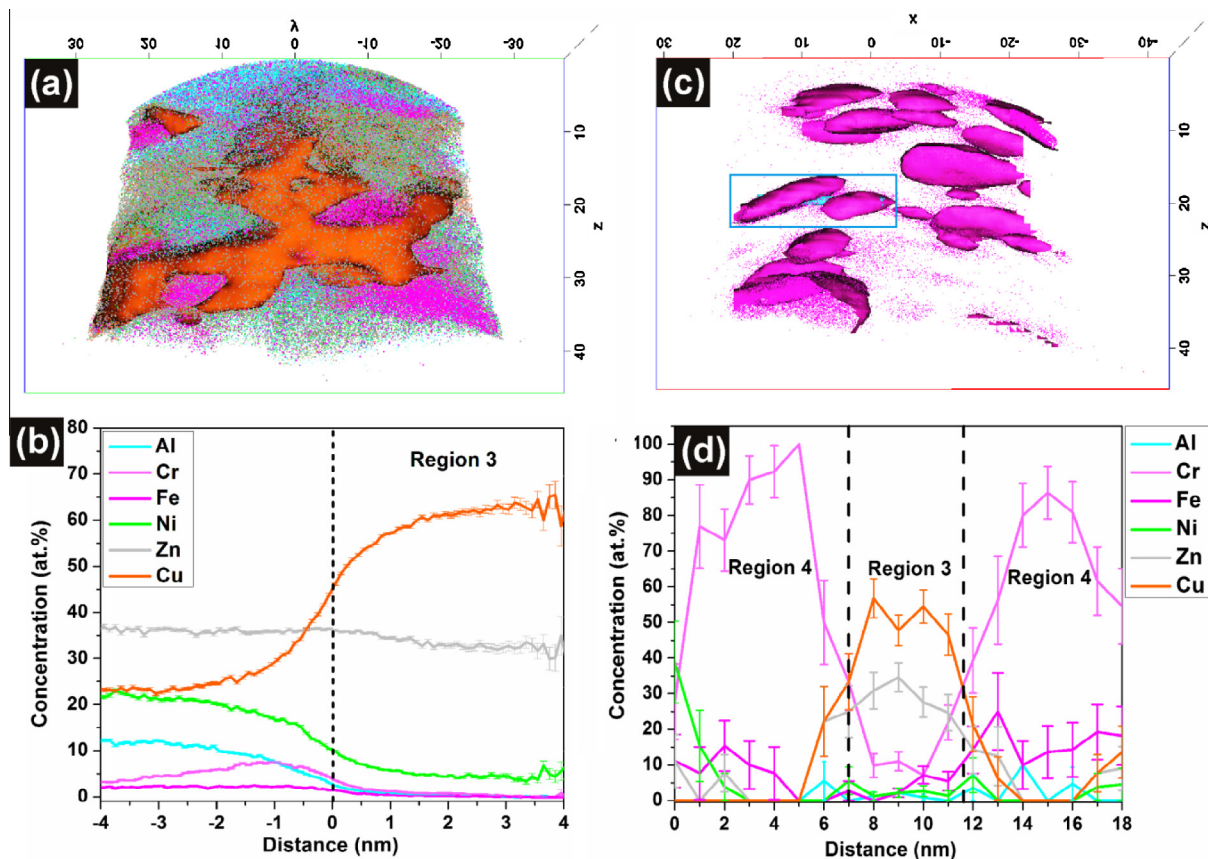


Fig. 8. APT elemental maps of: (a) Cu atoms [■] with isoconcentration surfaces (50 at.% Cu interface) showing a Cu–Zn phase; (b) corresponding proximity histogram of 0.15 nm bin size with respect to the Cu–Zn phase boundary; (c) Cr atoms [■] with iso-concentration surfaces (25 at.% Cr interface) showing Cr-rich precipitates and (d) concentration–depth profiles of all alloying elements determined with a cylinder of radius 0.65 nm (indicated by a marked rectangle in (c)). The profiles are plotted with a moving step of 1 nm from right to left. The dotted lines separate regions 4 and 3 enriched in Cr and Cu, respectively.

regions of Fe–Co-rich and Cr-rich domains has been reported in the as cast AlCoCrCuFeNi HEA [11]. This matches our present findings of the existence of a nearly pure Fe phase (region 2 in Fig. 5b) and a Cr-rich phase (Fig. 8c). Formation of such Cr-rich sigma phase (σ) after spark plasma sintering at 900 °C of the mechanically alloyed NiCoCrCuFe and NiCoCrFe HEA has also been reported [14], suggesting the possibility of similar decomposition behavior. Since the lattice parameter of bcc Cr is the same as that of the Ni–Al bcc phase ($a_{\text{bcc}} = 287$ pm) it is highly unlikely that they can be distinguished using diffraction techniques. Moreover, the chemical composition analysis and elemental mapping by TEM EDX may be unreliable in the current case as the crystallite size of the phases in the as-milled and hot compacted condition are extremely small, namely of the order of 11 ± 1 and 20 ± 8 nm, respectively.

The crystallite size of the HEA after hot compaction is only 20 ± 8 nm. The average values of the crystallite size obtained from TEM match those measured by XRD. Moreover, the presence of the characteristic ring pattern (Fig. 4b) also confirms the overall nanocrystalline nature of the hot compacted alloy. The reason for such high thermal stability of the nanocrystals could be associated with

the formation of an α -brass phase (Cu–30 at.% Zn) along the grain boundaries. The enrichment of Cu in α -brass is expected to exert a strong repulsive interaction [30] with other elements in the alloy except for Zn [20], thereby preventing the diffusion of elements between phases and hence controlling grain growth. This explains the presence of an almost pure Fe phase (96 at.%), (region 2 in Fig. 5a) adjoining the α -brass hetero-interphase. As a result the nanocrystalline microstructure of the alloy is stabilized by the Cu–Zn enrichments.

These results reveal that the nanostructure of the HEA under investigation has a composite microstructure consisting of alternating hard Ni–Al and Cr–Fe phases that are separated by a more ductile α -brass phase along the interfaces between these phase regions. The very high hardness of the AlCrCuFeNiZn HEA can be attributed to the nanocrystalline nature of the alloy and to the individual hardness of Ni–Al and Cr–Fe phases, which together constitute the bcc matrix phase [12–14].

The current results enable us to critically evaluate phase formation and dissociation kinetics in the HEA design concept. More specific, the results show that the thermodynamically stable state of a multicomponent solid-solution phase, competing with other phases of similar composition,

is determined by the Gibbs free energy of all competing phases [34–37] and not by the mixing entropy alone as stated by the original high-entropy concept.

5. Summary, conclusions and outlook

The equiatomic AlCrCuFeNiZn HEA, produced by mechanical alloying and hot compaction, was investigated using XRD, TEM and APT. XRD indicates the deformation-driven formation of a major bcc solid-solution phase with a lattice parameter of 287 pm after 20 h mechanical alloying. Upon hot compaction at 600 °C for 15 min a composite microstructure was observed. The material had significant fractions of fcc phase (i.e. up to 40 vol.% after hot compaction) along with a major bcc matrix phase consisting of stable nanocrystals (20 ± 8 nm in size). Further analysis by APT revealed that the bcc phase was comprised of two locally decomposed regions, namely Ni–Al and Cr–Fe, having identical structure and lattice parameters. The Ni–Al and Cr–Fe regions are separated along the grain boundaries by a ductile fcc α -brass interphase region consisting of 63 at.% Cu and 32 at.% Zn. Such α -brass segregations along the grain boundaries stabilize the nanostructure.

Irrespective of the material having highly stable nanostructures the primary objective of synthesizing a single-phase alloy and retaining the same nanostructure at high temperatures has not been realized. Moreover, in many previous cases, including the present alloy, the microstructural changes at the atomic scale upon annealing violate the HEA design principles where a homogeneous solid solution is targeted. We hence suggest a conceptual modification of the HEA design, considering that the Gibbs free energy determines the equilibrium state of an alloy, and not the mixing entropy alone. In order to achieve this criterion, the alloying elements considered must have high equilibrium solid-solubility limits among each other which can be determined using CALPHAD-type models.

Acknowledgements

The authors would like to thank Dr. Sheela Singh for stimulating discussions. K.G.P. is grateful for the financial support provided by the “DAAD-IIT Masters Sandwich Program” for his stay at HZB Berlin.

References

- [1] Ranganathan S. *Curr Sci* 2003;85:1404.
- [2] Tong CJ, Chen YL, Chen SK, Yeh JW, Shun TT, Tsau CH, et al. *Metal Mater Trans* 2005;A36:881.

- [3] Zhang Y, Zhou Y. *Mater Sci Forum* 2007;561–565:1337.
- [4] Yeh JW, Chen SK, Gan JY, Lin SJ, Chin TS, Shun TT, et al. *Metall Mater Trans A* 2004;35A:2533.
- [5] Guo S, Ng C, Lu J, Liu CT. *J Appl Phys* 2011;109:103505.
- [6] Tong CJ, Chen MR, Chen SK, Yeh JW, Shun TT, Lin SJ, et al. *Metall Mater Trans* 2005;36A:1263.
- [7] Yeh JW, Chen YL, Lin SJ, Chen SK. *Mater Sci Forum* 2007;560:1.
- [8] Tung CC, Yeh JW, Shun TT, Chen SK, Huang SY, Chen HC. *Mater Lett* 2007;61:1.
- [9] Singh S, Wanderka N, Murty BS, Glatzel U, Banhart J. *Acta Mater* 2011;59:182.
- [10] Manzoni A, Daoud H, Mondal S, van Smaalen S, Voelkl R, Glatzel U, et al. *J Alloys Compd* 2013;552:430.
- [11] Singh S, Wanderka N, Kiefer K, Siemensmeyer K, Banhart J. *Ultramicroscopy* 2011;111:619.
- [12] Varalakshmi S, Kamaraj M, Murty BS. *J Alloys Compd* 2008;460:253.
- [13] Varalakshmi S, Kamaraj M, Murty BS. *Mater Sci Eng A* 2010;527:1027.
- [14] Praveen S, Murty BS, Kottada RS. *Mater Sci Eng A* 2012;534:83.
- [15] Benedict JB, Anderson R, Klepeis SJ, Chaker N. *Mater Res Soc Proc* 1990;189–204.
- [16] Benedict JB, Anderson R, Klepeis SJ. *Mater Res Soc Proc* 1991;121–40.
- [17] Cullity BD. *Elements of X-ray diffraction*. 2nd ed. Reading, MA: Addison Wesley; 1978.
- [18] Miller MK, Cerezo A, Hetherington MG, Smith GDW. *Atom probe field ion microscopy*. Oxford: Clarendon Press; 1996.
- [19] Thompson K, Lawrence D, Larson DJ, Olson JD, Kelly TF, Gorman B. *Ultramicroscopy* 2007;107:131.
- [20] Hume-Rothery W. *Acta Metall* 1966;14:17.
- [21] Kittel C. *Introduction to solid state physics*. 6th ed. New York: John Wiley; 1980.
- [22] Hume-Rothery W. *Acta Metall* 1967;15:567.
- [23] Zhang Y, Zhou Y, Lin JP, Chen GL, Liaw PK. *Adv Eng Mater* 2008;10:534.
- [24] Raabe D, Choi PP, Li YJ, Kostka A, Sauvage X, Lecouturier F, et al. *MRS Bull* 2010;35:982.
- [25] Li YJ, Choi PP, Borchers C, Chen YZ, Goto S, Raabe D, et al. *Ultramicroscopy* 2011;111:628.
- [26] Li YJ, Choi PP, Borchers C, Westerkamp S, Goto S, Raabe D, et al. *Acta Mater* 2011;59:3965.
- [27] Ohsaki S, Raabe D, Hono K. *Acta Mater* 2009;57:5254.
- [28] Heringhaus F, Raabe D, Gottstein G. *Acta Metall* 1995;43:1467.
- [29] Raabe D, Mattissen D. *Acta Mater* 1998;46:5973.
- [30] Takeuchi A, Inoue A. *Mater Trans* 2005;46:2817.
- [31] ASM Handbook. Alloy phase diagram, vol. 3; 1992.
- [32] Porter DA, Easterling KE. *Phase transformations in metals and alloys*. 2nd ed. London: Chapman & Hall; 1992.
- [33] Chen YL, Hu YH, Hseih CA, Yeh JW, Chen SK. *J Alloys Compd* 2009;481:768.
- [34] Otto F, Yang Y, Bei H, George EP. *Acta Mater* 2013;61:2628–38.
- [35] Reeh S, Music D, Gebhardt T, Kasprzak M, Jaepel T, Zaefferer S, et al. *Acta Mater* 2012;60:6025.
- [36] Counts WA, Friák M, Raabe D, Neugebauer J. *Acta Mater* 2009;57:69.
- [37] Raabe D, Sander B, Friák M, Ma D, Neugebauer J. *Acta Mater* 2007;55:4475.